NeXT-Grenoble, the Neutron and X-ray tomograph in Grenoble

Alessandro Tengattini, Nicolas Lenoir, Edward Andò, Benjamin Giroud, Duncan Atkins, Jerome Beaucour, Gioacchino Viggiani

NeXT-Grenoble, the Neutron and X-ray Tomograph in Grenoble

Alessandro Tengattini[a,b,*], Nicolas Lenoir[a], Edward Andò[a], Benjamin Giroud[b], Duncan Atkins[b], Jerome Beaucour[b], Gioacchino Viggiani[a]

[a] *Univ. Grenoble Alpes, CNRS, Grenoble INP, 3SR, 38000 Grenoble, France*
[b] *Institut Laue-Langevin (ILL), 71 Avenue des Martyrs, 38000 Grenoble, France*

Abstract

NeXT-Grenoble is a Neutron and X-ray Tomograph launched from the collaboration between the Universite Grenoble Alpes (UGA) and the Institut Laue Langevin (ILL). The design started in February 2016 shortly followed by its construction at ILL. A first version of the instrument has been opened to users since October 2016.

One of the peculiarities of the instrument is that, as suggested by the name, the instrument allows the acquisition of *truly* simultaneous neutron and x-ray tomographies, taking advantage of the high complementarity of these two beams.

Also by virtue of the uniquely high flux at the ILL, the instrument can provide unprecedented spatial resolution (around 4 μm true resolution, in few tens of seconds) and acquisition speed (1.5 second tomographies).

This contribution details the adopted technical solutions and performances achieved, reviews some of the key published results and outlines the future direction of the instrument.

Keywords: Cold neutrons, X-ray, Imaging, Tomography, Dynamic Imaging, High Resolution

*Corresponding author
Email address: tengattini@ill.fr (Alessandro Tengattini)

1. Introduction

NeXT-Grenoble is a Neutron and X-ray Tomograph launched in 2016 from the joint effort of Université Grenoble Alpes, UGA (and specifically Laboratoire 3SR) and the Institut Laue-Langevin, ILL, and takes advantage of its world-leading neutron flux. Design started in February 2016 and the instrument was available to users in October 2016. It is currently fully open for proposals through its dedicated website https://next-grenoble.fr.

The high neutron flux available automatically makes this a unique instrument, since tomography performance (in terms of spatial resolution, temporal resolution and measurement noise) is wholly dependent by noise in data collection and therefore flux. Another key feature of the instrument is the possibility to perform x-ray absorption imaging, in order to take advantage of the high complementarity of these two techniques, sketched in Fig. 1. The design of the instrument is conceived with both fundamental and engineering studies in mind and therefore with the possibility of housing complex *in-situ* testing apparatus for a variety of thermo-chemo-hydro-mechanical experiments. The instrument uses a particularly "cold" beam (with flux peaking at 2.8 Å) which increases the contrast due to the energy dependence of the absorption cross-section, at the cost of a reduced penetration capacity. Neutron imaging has a broad range of applications ranging from renewable energies [1, 2, 3, 4] to biology [5, 6], and from paleontology [7, 8] to porous media [9, 10], as outlined in multiple review papers (*e.g.*, [11, 12])

In this paper we describe the layout of NeXT-Grenoble[1], the neutron and x-ray imaging equipment and their performances as well as a few selected ex-

[1] A note should be made about the name of the instrument, which is an acronym for **Ne**utron and **X**-ray **T**omography and which is partially shared with the neutron and x-ray imaging option in NIST, also named NeXT [13]. While, to the best of our knowledge, the name of NeXT-Grenoble might be shortly antecedent [14] to that at NIST, the overlap of the two names is a coincidence and the two instruments are not related. For sake of brevity in this text we will refer to the instrument interchangeably as NeXT and NeXT-Grenoble, albeit its full name is the latter. It should also be noted that, while the name of the instrument only includes the term "tomography," NeXT is currently capable of performing also other kinds of absorption imaging, and notably radiography.

amples of the published results achieved thus far. This paper is meant to be the principal reference for the current status of the instrument, superseding the previous one [14]. A significant upgrade of the instrument, including for example monochromation and polarisation options, is foreseen in 2021/2022, as detailed in Section 6. This might be followed by a dedicated publication on its novelties. No significant interruption of public availability is currently foreseen to perform this upgrade. For one of the more complex aspects of the facility, simultaneous x-ray and neutron imaging, a dedicated publication is under development. Therein theoretical considerations, technical details and practical applications will be more adequately explored. It goes without saying that the presented instrument benefits from the experience matured by the neutron imaging community, as well as the developments in synchrotron and lab scanners over the last decades, as detailed below.

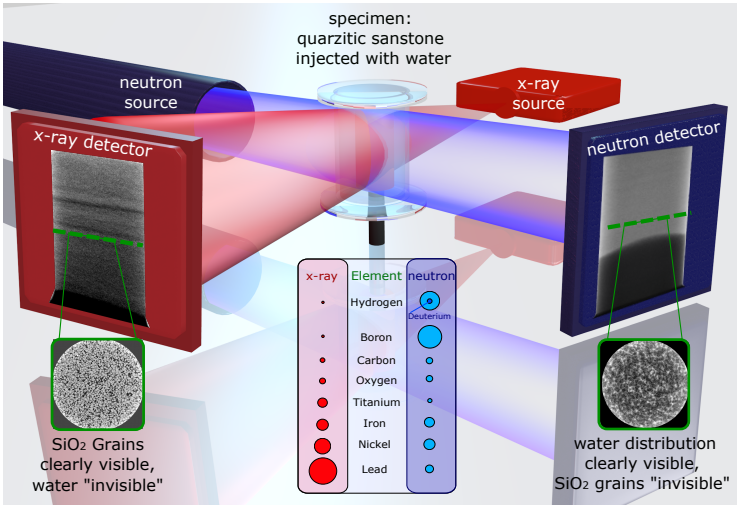

Figure 1: Sketch of the underlying concept of NeXT: the high complementarity of the two techniques generally makes the combination of the two superior to the sum of the parts [15]. In the example of *in-situ* testing of fluid flow in porous media, x-ray is ideal for detecting the solid skeleton and measuring its deformation whereas neutrons are best suited to study the hydraulic response.

2. Source and guides

Built in 1967 and refurbished between 1991 and 1995, the ILL is a heavy-water cooled and moderated swimming pool-type reactor, operating with a thermal power of 58.3 MW, which provides the most intense continuous neutron flux in the world (1.5×10^{15} n/cm^2/s in the moderator region).

NeXT is situated at the end of the H521 guide which is fed by the Horizontal Cold source SFH ("Source Froide Horizontale", in French). The H5 beam tube is followed by a 13 m long guide with a radius of 4000 m, then by a 30 m segment with 1500 m curvature and finally by 30 m of straight guide. All these segments ex-pile are supermirror-coated for m=2. This relatively uncommon curvature significantly reduces the amount of thermal neutrons and gamma radiation produced in the reactor reaching the instrument.

The location of the instrument within the ILL is shown in Fig. 2. The H521 guide starts with a 117x120 mm rectangular section, which becomes a 150x60 mm section after about 20 m, which is then maintained in the last 28 m. Two pneumatic safety shutters made of boron carbide and lead are positioned immediately at the end of H521 and 5 m behind it.

From this rectangular guide only a 30 mm circle in the topmost section is currently used for imaging, although more will be used in future upgrades (which will be detailed in section 6).

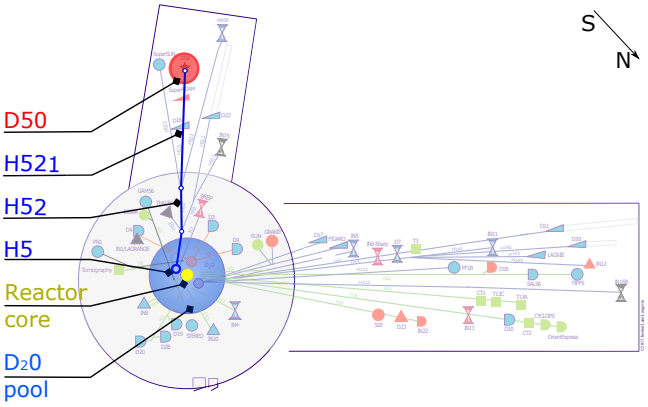

Figure 2: Schematic plan of all instruments at ILL, highlighting the position of NeXT-Grenoble. Modified from https://www.ill.eu/users/instruments/.

3. Instrument layout

At the end of the H521 cold guide lies the "D50" experimental station. It currently houses two separate instruments/configurations: the Neutron and X-ray Tomograph (NeXT-Grenoble), which is the object of this paper, as well as the Rainbows reflectometer described in [16]. In brief, the peculiarity of this reflectometer is that instead of using the more traditional time of flight approach to discern the wavelength of neutrons, it takes advantage of the wavelength-dependency of their deflection by a prism. The wavelengths are then measured with a high spatial resolution detector. The construction of the reflectometer was initiated in 2014, and financed by the French government initiative "Programme d'Investissement d'Avenir" funded by the IRT Nanoelec and more specifically by its program led by the ILL, dedicated to bridge the gap between industry and large scale research facilities. As aforementioned, the imaging station was added in 2016, financed by the Université Grenoble Alpes. The two instruments, sketched in Fig. 3, currently work in alternation, as detailed below.

At the end of the guide lie both a set of sintered B4C pinholes for the tomograph (30, 23, 15, 12.5, 10, 7 and 5 and 2.5 mm in diameter), as well as a number of vertical slits for the reflectometer. Additionally, a pneumatic

fast shutter made of boron carbide as well as two graphite filters (5 mm and 10 mm thick) can be positioned in the beam. Further downstream, there are two 5 m long parallel vacuum flight tubes, optimised for imaging and reflectometry respectively. The tubes are placed on a rail which allows their alignment with the neutron beam depending on the operation mode.

Rainbows reflectometry employs the wavelength-dependent deflection of a prism to study the reflective properties of matter employing the full white beam, which is detected at 4 m from the sample with a scintillator-based detector as sketched in Fig. 4. When the instrument is operated in Imaging mode, all the reflectometry components are either removed or displaced sideways to allow for an additional 5 m long vacuum flight tube to be added along the beam path.

In summary, for the purpose of this work, the end of the neutron guide is followed by a series of beam shapers and then by a 10 m long flight tube, which leads to the imaging station itself. The radioprotective bunker of the tomograph is made of modular concrete blocks (unlike the rest of the instruments upstream whose shielding is made from lead and B4C) to simplify the compliance with the amagnetic constraints of a neighbouring instrument (the spin-echo spectrometer "WASP"). The roof is made of long concrete beams which can be rapidly removed by crane for the installation of large pieces of equipment in the bunker.

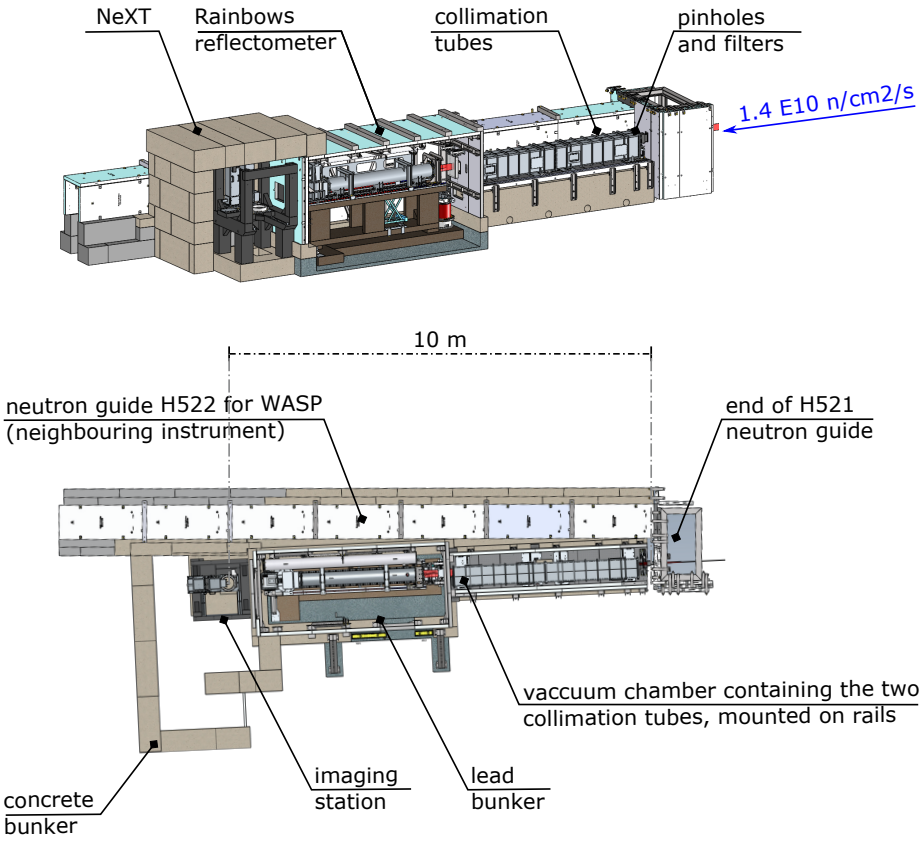

Figure 3: Side and top view of the D50 instrument in its entirety, including the tomograph and the reflectometer

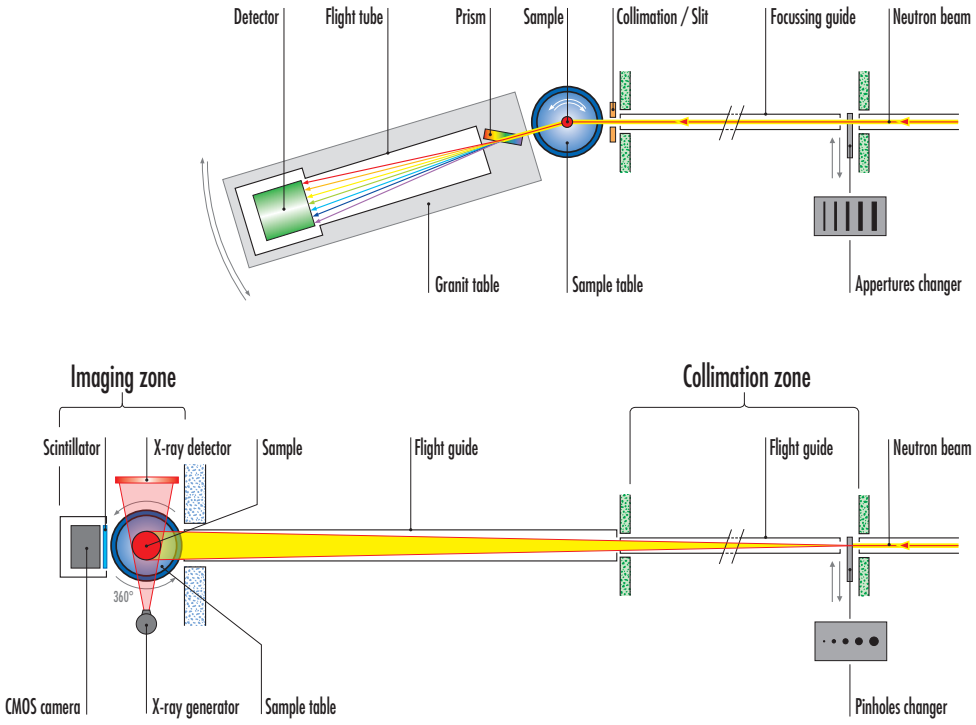

Figure 4: Conceptual description of the two components of D50: the rainbows reflectometer (top) and the tomograph (bottom). From https://www.ill.eu/users/instruments/instruments-list/d50/description/instrument-layout/. It should be noted that after the neutron guide and shutters no element is in common between the two instruments. A 10-meter beam collimation tube is placed in lieu of all the elements in the top part of the figure as detailed in the text.

3.1. Beam characteristics

The flux, as measured by gold foil, at the end of the H521 guide is of 1.4×10^{10} n/cm^2/s, which, to the best of the authors' knowledge, makes NeXT-Grenoble the imaging station with the highest neutron flux in the world. With the largest pinhole currently available, the maximum flux at the sample position is of 3×10^8 n/cm^2/s for an L/D of 333 at the sample position, and future

upgrades (Section 6) intend to explore the higher flux at lower L/D ratios. To compare it to other notable facilities for an arbitrary collimation ratio L/D of 400, at FRM2 (ANTARES beamline) there is a reported flux of 1×10^8 n/cm^2/s (without any of the elements available to reduce fast neutron and gamma background), while NIST (BT-2 beamline) the flux is of about 6×10^7 n/cm^2/s (without the Beryllium filter) and at PSI (ICON beamline) it would be of about 1×10^7 n/cm^2/s (as *estimated* from a reported 1.3×10^7 n/cm^2/s for an L/D of 343). At ILL for the collimation ratio L/D of 400 the flux would be of about 2×10^8 n/cm^2/s) [17, 18, 19, 20].

The spectrum peaks around 11 meV, corresponding to a wavelength of 2.8 Å as highlighted in Fig. 5. This spectrum was measured by the reflectometer, 5 m from the end of the guide. The two visible dips in the spectrum at 4.518 Å and 5.241 Å are caused by two fixed monochromators upstream as part respectively of the D16 diffractometer [21] and the SuperADAM reflectometer [22].

The beam is not perfectly homogeneous, as highlighted in Fig. 6 (a). Figs. 6 (b) and (c) show the vertical and horizontal profiles of the beam intensity of the central part of the beam for a selection of the available pinholes. These profiles highlight how the beam is relatively homogeneous (above 70 % of the maximum value) within the central 100 mm and that the larger pinholes generate a slightly more homogeneous beam than the smaller ones. Some of the finer details of this inhomogeneity are induced by the limited reflection at the joints of the beam guides upstream, and can be partly compensated by employing the graphite filters detailed in section 3.

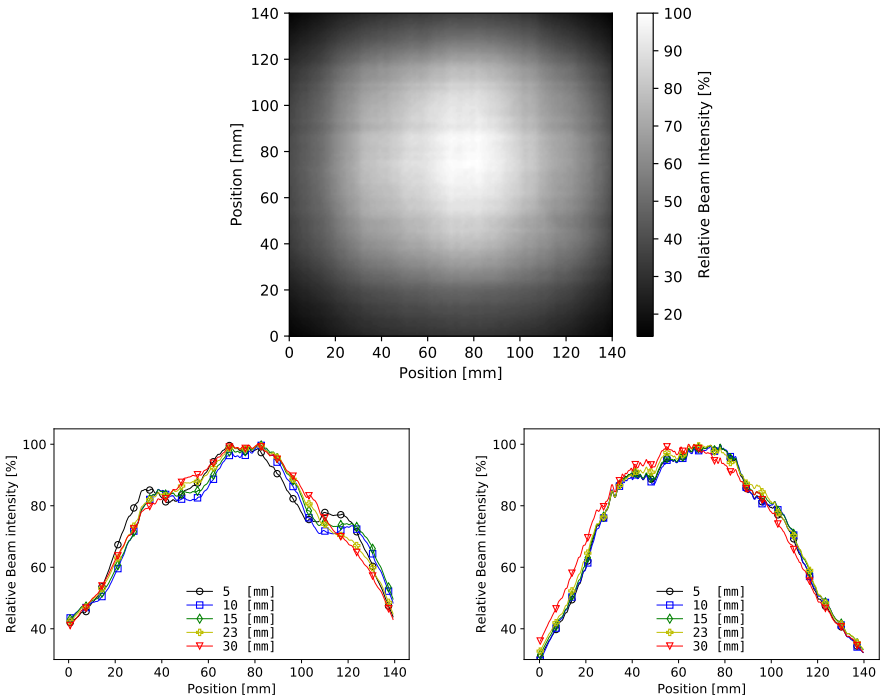

Figure 6: Map of the beam distribution (a) Horizontal (b) and Vertical (c) profiles of the central 140 mm of beam intensity for different pinholes.

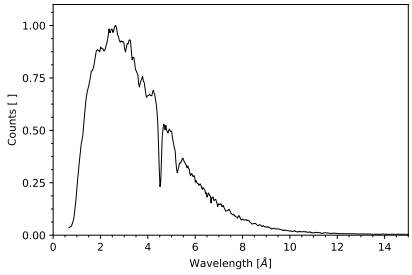

Figure 5: The neutron spectrum at NeXT, as determined by the Rainbows reflectometer introduced in section 3. The used method might justify some of the higher frequency fluctuations in the plot.

4. Imaging station

4.1. Neutron detectors

Three neutron detectors are currently available at NeXT: a medium resolution detector, with a continuously variable field of view, detailed in section 4.1.1 and two high resolution detectors, each optically optimised for a discrete number of fields of view, detailed in section 4.1.2. The detectors are mounted onto a rotating plate which allows for the swapping of two positions, one with the medium resolution detector and one which allows for mounting either of the high resolution detectors with high repeatability thanks to high accuracy dowel pins.

4.1.1. Medium resolution detector

The Medium Resolution detector at NeXT, shown in Fig. 7, follows a common approach in neutron imaging: scintillator, mirror and camera plus optics.

One of the peculiarities of this detector is the fact that the scintillators can be mounted onto protruding "noses". This is meant to allow minimal distance between sample and detector (to reduce the so called penumbra blurring thus maximising the true spatial resolution) in the case of complex sample environments (*e.g.*, flanged mechanical testing rigs, where the cell diameter in the middle region can be significantly smaller than at its extremities), in line with the user-oriented philosophy of the instrument. Multiple available noses of different sizes can be mounted on the detector to allow for different scintillator/mirror distance as well as different scintillator sizes. The scintillators are held in place by a counterframe screwed on the nose itself, which also ensures light-tightness. This elongated nose also removes the risk of multiple reflections between mirror and scintillator. This detector has its longest axis oriented vertically to minimise the encumbrance in the working plane.

At the moment of this writing, the set of available scintillators includes $ZnS/^6LiF$ scintillators of different thicknesses (200, 100 and 50 µm), as well Gadolinium Oxysulfides (20, 10, 5 µm $Gd^2O^2S : Tb/^6LiF$ and a 3 µm one, this

latter one enriched with the isotope 157 of Gadolinium: $^{157}Gd^2O^2S : Tb$ as detailed in [23]). These gadolinium scintillators can also be (and are predominantly) used in the high resolution detectors detailed in the next section. Given the high neutron flux, their efficiency decreases with time and they are therefore periodically replaced, and new scintillators of different sizes, thicknesses and compositions will be added to the above set, depending on the necessities.

A mirror is placed behind the scintillator at an angle of 45°, held by a mechanically adjustable frame, which ensures a 90° image reflection. This common solution is adopted to keep the camera electronics out of the primary beam in order to minimise radiation damage. While the choice of the mirror was initially optimised for optical efficiency, this has resulted in a relatively high gamma count near the camera which can reduce its life expectancy, increase noise and induce occasional camera errors. Currently a 0.5 mm thick SiO_2 wafer coated by pure aluminium layer is used as a mirror, with a noticeable reduction of measured gammas, and an acceptable loss of light.

Images are acquired by a Hamamatsu ORCA-Flash4.0 V2 sCMOS camera, which is actively water cooled. This camera has an array of 2048x2048 pixels 6.5 µm in size. In this case a sCMOS camera was chosen over a CCD for the higher (100 Hz) maximum reading speed, essential given the high flux of the instrument, albeit the addition of a new CCD camera for the higher resolution is planned in the future. This camera can mount a set of lenses including a 24 mm f./0.9, 50 mm f./1.2, 60 mm macro f./2.8, 85 mm f./1.2, 100 mm f./2.0 macro, 105 mm f./1.4 , 180 mm macro f./3.5 as well as 1.4x and 2.0x teleconverters, for a continuous range of fields of view from 165 mm × 165 mm down to potentially below 20 mm × 20 mm (although below 30 mm the high resolution setups are optically more efficient) as highlighted in Fig. 8.

The camera is mounted on a high accuracy rail (nominally ±3 µm position repeatability) coupled with a high precision optical encoder (down to 50 nm), which permits the adjustment of the field of view as well as to finely tune the focus. The entire mechanics (choice of granite as construction material, as well as the high accuracy of the linear actuators and encoders down to few

microns in accuracy and repeatability as will also be the case for the x-ray setup in section 4.2) was conceived for thermal and mechanical stability of the setup to enable the desired high spatial resolutions across a tomography in a non-temperature controlled bunker, as well as for experimental repeatability. Once the manual pre-focusing is performed with an optical target, a number of images of a known target at regularly spaced camera positions are acquired. Their frequency content is then analysed to determine the sharpest image and therefore the optimal focusing position. The high reproducibility of the setup permits to then go back to this ideal position. The highest spatial resolution achieved with this setup is of 30 µm.

The setup is encased within a box which ensures light tightness including light-tight sheaths to pass the control cables. Multiple 2 cm thick lead sheets coupled with 0.5 mm boron carbide sheets are then used to further reduce the radiation damage to the optical components.

To have a *general indication* of the overall efficiency of this setup, it takes 0.5 s to almost saturate the camera in binning 1 using a 100 µm $ZnS/^6LiF$ scintillator, for a field of view of about 100 mm (using the 50 mm lens). This implies that in binning 4 it takes indicatively 30 ms to almost saturate the camera, (*i.e.* the signal to noise ratio goes below 10 only around 1 ms exposure). This in turn implies that fast tomographies composed for example of 200 or 300 projections can be acquired with sub-second exposures. For example the tomographies in Fig. 11 are a recent result from [24], and were acquired in 1.5 s, highlighting a water imbibition front in a loose soil containing Lupine roots, underlining the potential of the technique for imaging of high speed processes.

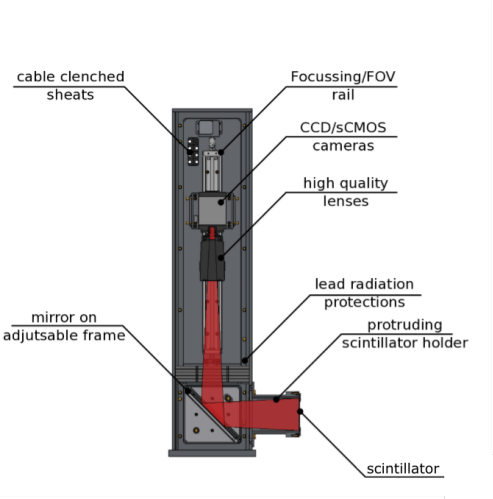

Figure 7: Commented design of the medium resolution detector at NeXT.

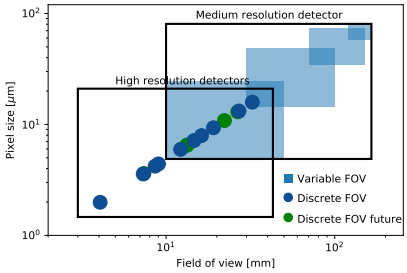

Figure 8: Range of available (and forthcoming) fields of view and corresponding pixel sizes achievable with the medium resolution and the suite of high resolution detectors

4.1.2. High resolution setups

To achieve better spatial resolutions, a higher degree of collimation (L/D, where L is the pinhole/sample distance and D is the pinhole size) of the beam is necessary, which reduces the effective neutron density at the sample position. Additionally, given the higher magnification required, the density of neutrons *per pixel* per second is also reduced. Smaller effective pixel size also requires higher magnification lenses which have a lower numerical aperture (their photon acceptance). Finally, the higher light output scintillators (*e.g.*, the $ZnS/^6LiF$ ones) cannot be employed : in these scintillators, in fact, the capture process

begins with the activation of 6Li, which emits triton and alpha particles, exciting the ZnS, which in turn emits photons. The mean free path for these triton particles in Li6/ZnS is 130 µm, which is incompatible with higher resolutions. Conversely, Gadox scintillation works through electrons whose mean free path is 12 µm. The drawback is that while 10 µm of Gd can stop 90 % of the beam, the photon emission per neutron is orders of magnitude lower than Li:F scintillators.

Consequently, while the detector detailed in the previous section could in principle be adopted for higher resolutions, the exposure times rapidly becomes unsustainable. The approach followed here for the higher resolutions is therefore to adopt optically optimised solutions covering a number of discrete fields of view (rather than allowing its continuous variation as for the medium resolution detector) to partially compensate for the lower photon flux. It makes use of the infinity corrected optics approach described in [25, 26, 27] and adopted in other leading centres such as the Helmholtz Zentrum Berlin (from which this design was inspired).

It employs an "imaging lens" (usually a telephoto or tube lens) to form a parallel light image which is then captured by one of the high aperture "objective lenses" detailed above. NeXT-Grenoble currently employs two setups relying on one of two right-angle lenses manufactured by Rodenstock: an XR-Heliflex f = 122 mm f/2.6 (Numerical Aperture NA = 0.2) and a TV-Heliflex f = 55 mm, f/1.0, (NA = 0.41), with a third, intermediate detector mounting an XR-Heliflex f = 100 mm, f/1.50, (NA = 0.32) currently under construction.

Depending on the combination of imaging and objective lenses used, the *effective* pixel size changes. This is usually expressed through the magnification factor M, which in this case is simply the ratio between the focal lengths of the Objective and the Imaging lenses. One of the several possible configurations allowed by this setup, combines the 55 mm TV-Heliflex, coupled with the 180 mm Canon objective lens, which yields a magnification factor of 3.27, which, when the Hamamatsu ORCA sCMOS camera detailed above is used, gives a virtual pixel size of 6.5/3.27=1.99 µm. A list of possible combinations of the lenses and ensuing resolutions and fields of view is reported in Table 1. While zoom lenses

Obj Lens	Img. Lens	Magnification	pixel size [µm]	FOV [mm^2]
50	122	0.41	15.86	32.48x32.48
50	55	0.90	7.15	14.64x14.64
100	55	1.81	3.58	7.32x7.32
180	55	3.27	1.99	4.06x4.06

Table 1: Magnification (M), effective pixel size (P_{eff}), and Field of View (FOV) for several combinations of available objective/imaging lenses.

could be adopted for this setup, allowing intermediate fields of view, these lenses have generally a lower numerical aperture, which increases the exposure time and lower sharpness.

Fig. 9a shows a rendering of the detector mounting a 55 mm TV-Heliflex in a configuration coupling it with a the 50 mm f./1.2 Canon (*i.e.* in this case the virtual and real pixel sizes coincide). Unique to this design is the possibility to change the objective lenses while maintaining the distance to the imaging lens constant, essential to minimise photon losses. Different scintillators can be mounted on either detectors. The design allows the minimisation of the sample/detector distance by virtue of the shape of the scintillator holder as well any potential interactions with the x-ray setup thanks to the compact design and to the possibility to orient the detector in three different positions (with camera to the right, the left or above the beam).

At the moment of this writing this setup achieves a resolution of about 4 µm, as highlighted in Figure 9b. This compares favourably with the existing results from the literature. For example, the PSI Neutron Microscope Project [28] follows a classic scintillator/mirror/lens design but adopts a bespoke, high numerical aperture lens with a fixed focal length. To the best of the authors' knowledge its current highest resolution of 4.5 µm was achieved based on 40 individual radiographs over about 20 minutes when it was recently tested at the Institut Laue Langevin [29]. Approaches based on single event reconstruction [30] provide spatial resolutions as low as 2 µm, albeit coming at the cost of the acquisition of about 10^5 frames, which, with the current technology, translates

to more than one hour per radiograph, not accounting for the time needed for the data treatment as centroid recuperation. This was achieved by combining the 55 mm TV-Heliflex lens, the 180 mm objective and the 3 µm $^{157}Gd^2O^2S:Tb$ scintillator detailed in [23] and produced and sold by the Paul Scherrer Institute.

To provide a *general indication* of the overall efficiency of this setup, it takes less than one minute to saturate the 16 bit camera with a standard 5 µm $Gd^2O^2S:Tb$ scintillator and an effective pixel size of 3.2 µm pixel size, yielding a 7 µm resolution (55 mm TV-Heliflex, 100 mm f/2.0 Zeiss lens). This would be about twice as long with the setup yielding a 4 µm resolution.

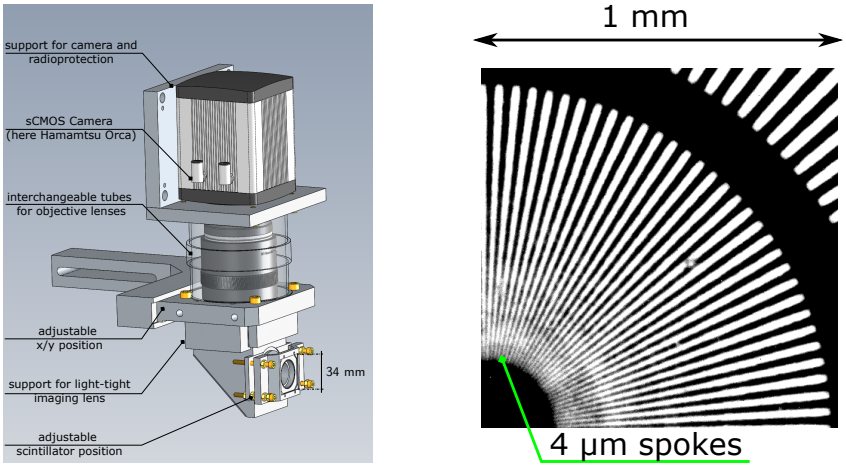

(a) **(b)**

Figure 9: Commented design of the high resolution detector at NeXT (a). The highest spatial resolution achieved, around 4 µm, is highlighted by the visible 4 µm spokes at the centre of the Siemens Star target produced and sold by PSI [31] in (b).

4.2. X-ray setup

The x-ray setup is constituted by a microfocus x-ray generator, a detector as well as by the corresponding mechanics, as highlighted in Fig. 10a.

The x-ray source is a Hamamatsu L12161-07, a sealed microfocus source with a Tungsten target and a Beryllium window. It can accelerate electrons towards the target with up to 150 kV and up to 500 µA, with a minimal focal spot size of 5 µm. To maximise the lifetime of the source by reducing the damage caused by

any scattered neutron, the source is encased by an aluminium box containing 6 mm of lead and 10 mm of boron carbide except in the exact point of exit of the beam, where a removable boron carbide plaque is placed.

The detector is a Varex PaxScan® 2530HE, where the HE stands for "High Energy". In this particular model in fact the electronics is moved to the sides of the active area of the detector (rather than behind it). This allows the masking of the electronics with additional shielding, for nominal use above 225 kV. In our case, a supplementary aluminium frame was installed to allow the addition of an extra sheet of 6 mm of lead as well as 10 mm sheets of boron carbide to cover the deported electronics. The active area of the detector also has a protective layer of 5 mm of Boron Carbide which only reduces the x-ray flux by a few percent while attenuating 99.9 % of the scattered neutrons. The use of lithiated polyethylene was also tested with comparable effects. These additional protections are particularly important at ILL, given the flux. The detector has 1792 x 2176 pixels 139 µm × 139 µm in size and is oriented in portrait mode, and has a maximum speed of 9 Hz (or 33 Hz in binning 2).

The scintillator chosen was Caesium Iodide (rather than the Gadolinium Oxide one) following the logic that the Gadolinium oxide one is also very sensitive to neutrons, meaning that it would more promptly detect unwanted neutrons scattered towards the flat panel. Furthermore, Caesium Iodide scintillators are more efficient than Gadolinium Oxide ones at higher x-ray energies, which is coherent with the types of samples more likely to be tested at NeXT.

It should be noted that the choice of the source and detector adopted, as well as of multiple other details regarding the x-ray setup, follows the successful example of the laboratory scanner of Laboratoire 3SR, partner in the development of this instrument [32].

The source and detector are mounted onto a granite arch (as shown in Fig. 10 a) and their distance is step-wise fixed (the source holder allows for four different position 20 mm apart). The shortest distance is of 500 mm, chosen to be slightly larger to the maximum illuminated area given the 43° of opening of the beam, and by geometrical considerations. The zoom is made possible by an axis moving

this ensemble with respect to the sample. This ensemble can also pivot by ±20° to reduce the cross-talk between the x-ray and the neutron setup as well as be moved into a "parking position" beside the neutron flight tube.

This setup can achieve spatial resolutions as small as 5 µm and fields of view in principle almost as large as the 30 cm × 25 cm detector depending on the geometry of the object. Further details about the setup including the reasoning behind these technological choices, the cross-talk between techniques, the overall calibration of the setup and the data integration go beyond the purpose of this paper and will be detailed in a future publication.

NeXT-Grenoble, whose x-ray capabilities were added less than one year after its entrance into operation (*i.e.*, in 2017 [14]), is not the only instrument allowing for simultaneous x-ray and neutron imaging. The aforementioned BT2 instrument at NIST also allows for simultaneous x-ray imaging, and first instrument description was published around the same period (*e.g.*, [13], albeit some abstracts reporting the use of the technique date to 2016). PSI started instead introducing the possibility for combined x-ray and neutron imaging in 2015, with early results in 2016, as detailed in [33, 34].

It should be noted that in all these setups the x-ray capabilities are comparable to those of commercial μ-CT scanners, with resolutions around a few micro-meters. At the moment of this writing, several commercial x-ray scanners allow for significantly higher resolutions, even in the hundreds of nanometer range, allowing studies at spatial and temporal scales inaccessible to neutrons. While this is of great interest for numerous scientific problems, it comes at the cost of higher thermal and mechanical constraints, and can limit the possibility of a direct comparison between the x-ray and neutron images, which justifies the choice of the setup detailed above.

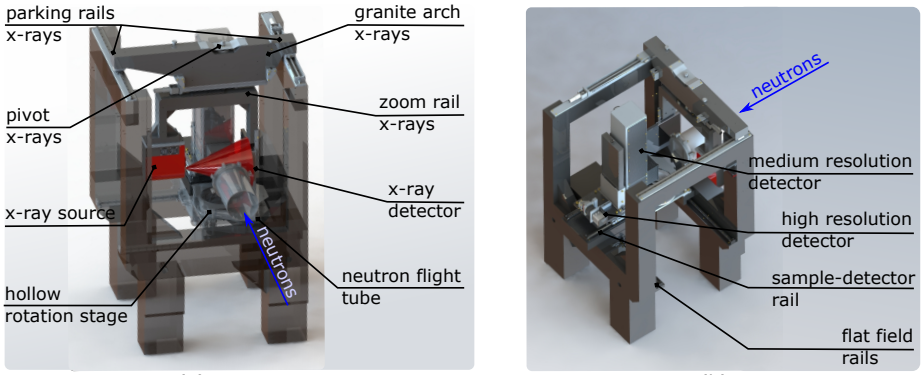

Figure 10: Design of the sample station highlighting the x-ray setup (a) and the neutron detectors (b).

4.3. Sample environment

The aforementioned x-ray and neutron setups are mounted on the granite structure in Fig. 10 and at https://youtu.be/4gPLJsk-9Ig. Granite was chosen for its thermal and mechanical stability, essential given the high spatial resolutions sought and the current lack of thermal buffers to the environmental temperature variations of the hall. One of the unique aspects of the setup is the adoption of a large, hollow rotation table (350 mm inner diameter). This allows for a variety of complex thermo-chemo-hydro-mechanical testing rigs to be installed with ease. Some sample environments can require heavy and cumbersome equipment, which is best placed below the rotation table where its weight stabilises the setup. This also allows the thickness of most apparatus (*e.g.*, triaxial, tension, flow rigs) to be minimised since the cell only needs to withstand the imposed loads. To maximise the space available to the testing rigs the rotation stage is therefore placed 1050 mm from the ground (*i.e.*, 260 mm below the centre of the beam, which is at 1310 mm from the ground) and an additional rectangular hole 450 mm deep is carved in the floor underneath it. The table can nominally withstand loads up to 500 kg with ± 5.0 millidegree accuracy.

An especially designed vertical axis allows for up to 90 mm vertical displacement without encumbering the region underneath the hole of the table. A

number of hollow or solid interface plates as well as an x, y, z and tilt axes can be added on top of the rotation stage depending on the application.

To acquire "open beam" or "flat field" images with ease, the rotation stage and the granite slab to which it is attached are mounted on rails moving both transversely to the neutron beam. The detectors are on a rail system, which allows the regulation of their distance to the sample position.

Near the sample environment a number of experiment infrastructure are available including AC (220 V and 380 V) and tunable DC electrical supplies (0-30 V, 0-3 A), exhaust gases recuperation system, compressed air (700 kPa), industrial input and output water systems, USB and Ethernet cables, monitoring cameras *etc.* Additional external gas bottle supply pipes and corresponding monitors (*e.g.*, hydrogen) are also currently under development.

4.4. Control software

The motion components, cameras, x-ray source and detector are all controlled by a user-friendly adaptive graphical user interface (GUI) specially developed with imaging in mind by the company RX-Solutions (France) over the past 15 years (https://www.rxsolutions.fr/). This software, initially developed for x-ray imaging, was adapted and optimised for combined x-ray and neutron acquisitions in collaboration with this company. This Qt, C++ based software allows a live flat and dark-field image correction, has a live 3D CAD model of the current position of all axes, can be controlled by both user interface and command line and is fully scriptable. Most importantly, the setup is fully calibrated so that the reconstruction parameters and pixel size are known for any given axis combination for both the x-ray and the neutron tomographies.

5. Selected examples of early results

Roughly eight months after the beginning of the design stage, a first iteration of the instrument was operational and open to early access users. Some of these early works have already been published and selected highlights are reported here to provide a glimpse of the capabilities and potential of the instrument.

In the context of natural resource exploitation, *e.g.*, hydrocarbon and water production or CO_2 sequestration, the high attenuation of hydrogen to neutrons offers an ideal contrast, for example to study the permeability field in dry porous media. Additionally, the isotope sensitivity of neutrons can be exloited, for example to follow alternate flushes of normal and heavy water while performing mechanical loading of porous materials. This method, pioneered in [35] has been adopted for explorations on multiple materials at NeXT, and some of the results obtained are presented in [36, 37]. The high flux available at ILL allows the acquisition of tomographies as fast as 1.5 s [24] while still having enough contrast to discern the two isotopes as well as the material structure. For example, Fig. 12a highlights the complexity of the flow path in a pre-compressed laminite sample. In this case, the speed of the process calls for the fast imaging capabilities unique to this instrument.

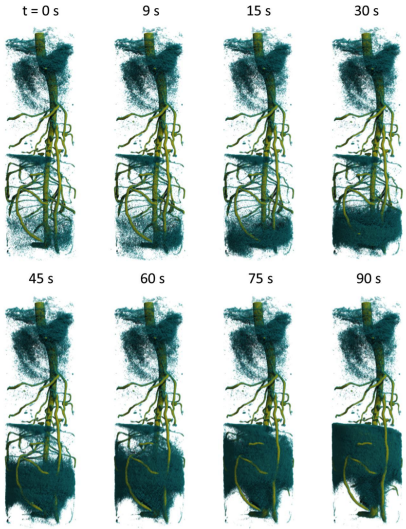

Figure 11: 1.5 s tomography of Lupine roots with a water front, from [24]

While hydromechanical experiments in sandstone/limestone require *relatively* low confinements, probing the response of concrete (*e.g.*, for dam or infrastructure durability analyses) can require to go up to several tens of MPa.

In [38] a newly developed Hassler cell capable of withstanding up to 90 MPa confining pressure is presented. In this case, the high flux of NeXT-Grenoble can penetrate through the thick (3 cm) titanium walls allowing the study of the hydraulic behaviour of concrete in real time and at high confinement.

A similarly complex high pressure apparatus is also required to hydraulically fracture rocks (*e.g.*, shales) for hydrocarbon exploitation, geothermal energy extraction as well as to study the influence of water pressure in the initiation of earthquakes. In [39] neutron imaging is employed to study the very fast process of hydraulic fractures initiation in a Marcellus shale at 30 MPa confinement, and the influence that bedding planes have on it. An example of the natural and induced fractures is reported in Fig. 12b.

The converse to these fluid flow problems is drying, key for example in the understanding of the fire response of concrete, which was studied in [10] and is shown in Fig. 12c. Once again the underlying process is intrinsically rapid and strongly heterogenous, making rapid neutron *tomography* the ideal tool. Concrete is a material of particular interest in porous media and an excellent example of the high complementary of the information which can be obtained combining x-ray and neutrons, as highlighted in Fig. 12d

Another example of the high complementary of x-ray and neutrons is the work of [9], where the hydro-mechanical response of a Callovo Oxfordian claystone is studied combining the high opacity of hydrogen to neutrons with the spatio-temporal resolution and density contrast of x-ray, as shown in Fig. 12e.

It goes without saying that, much in the same way early 4D datasets required the development of new analysis algorithms as DVC, new algorithmic developments are equally required to quantitatively interpret combined x-ray and neutron data. For example, in [15] novel theoretical developments, extending classical digital volume correlation are proposed. These allow the accurate (and user-independent) registration of two images acquired with different modalities, and thus exhibiting different contrast. As a *byproduct* of this procedure it is also possible to automatically segment the phases by analysing the joint x-ray and neutron histogram of the registered images. A recent paper by [40] details

the underlying technical aspects of the algorithm proposed by [15], applying it to neutron and x-ray tomographies of concrete as that in 12d. This yields a registered neutron image that matches the x-ray image with *sub-pixel* accuracy. Furthermore, a theoretical hydromechanical model exploiting both x-rays (to measured volumetric strain) and neutrons (water movement) has been recently proposed, which presents an interesting direction for future quantitative studies [41].

This instrument is fully open to public access, with submission through the website `https://next-grenoble.fr/`. As mentioned, the project was co-developed by the Université Grenoble Alpes, and specifically the Laboratoire 3SR, which focuses on the behaviour of porous media. This research centre has focused for the last fifteen years on imaging and the on the contributions it can provide to the understanding of the chemo-thermo-hydro-mechanical response (*e.g.*, [42, 43, 44]) of porous media. It is therefore unsurprising that most of these *early* works, developed during the commissioning phase, focus on the behaviour of porous media, although the full spectrum of areas of neutron imaging applications is of course of interest to the instrument and will be part of upcoming publications.

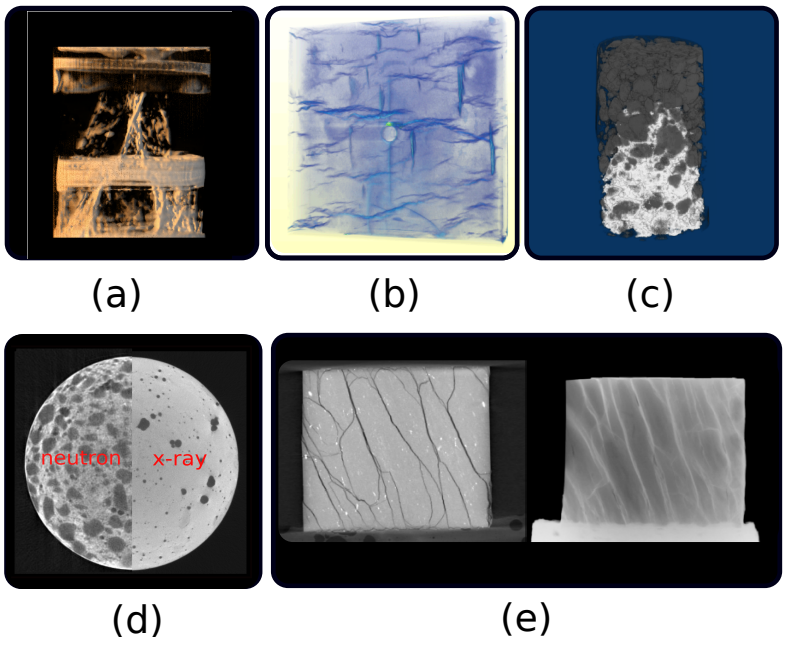

Figure 12: Selected examples of the capabilities of the instrument from published results. Example of a 2 min tomography of a complex permeability network of a laminite sample flushed *in-situ* [37] (a). Tomography of a shale sample after a 30 MPa fluid injection highlighting the natural and hydraulic-fracturing induced fractures [39]. Example of a 1 min tomography of a concrete sample subjected to an unidirectional 500° heating *in-situ* [10] highlighting in white the receding moisture profile and in black the aggregates (c), whose detection is simplified by the combined use of x-ray and neutrons [15] (d). The higher x-ray flux and density sensitivity also allows the complex hydromechanical behaviour of a water absorption of Callovo Oxfordian Claystone to be quantified by a combination of *in-situ* x-ray tomographies and neutron radiographies [9] (e).

6. Summary and future outlook

NeXT-Grenoble combines the world-leading flux of the ILL with high performance detectors, a high stability sample environment conceived for *in-situ* testing as well as a highly complementary x-ray setup allowing for fully simultaneous bi-modal acquisition.

The version of the instrument detailed above focuses on white beam cold neutrons and x-ray imaging. Additionally, it currently shares the available ILL beam-time with a rainbows reflectometer.

Thanks to the technical accomplishments and the high demand, the team involved has recently secured funding for a major upgrade of the instrument, within the Endurance Phase II program of ILL, which is expected to be delivered in 2021/2022. The instrument will become a standard ILL public instrument, thus accessing the entirety of available beamtime, available through the ILL proposal system. This new upgraded instrument will maintain the collaboration with the Université Grenoble Alpes with the addition of a partnership with the Helmholtz-Zentrum Berlin, including the integration of components and developments from the CONRAD-II imaging instrument [45, 46].

The future plan of the instrument, sketched in Fig. 13, foresees the addition of energy selective options (double crystal monochromator, velocity selector), polarised neutron imaging as well as grating interferometry, and generally the improvement of user facilities and instrument performance. These upgrades open a plethora of new options to tackle a variety of open scientific questions, as detailed by recent reviews focussing on advanced neutron imaging techniques (*e.g.*, [12, 45, 11]). For example, energy selective options [47] allow an enhancement in element sensitivity, provide insight into phase distributions in structural metals and geomaterials and give access to structural phase transitions end even strain fields [48]. Grating interferometry decouples angular and spatial resolutions and allows for detecting phase contrast (*i.e.*, shift of phase due to refraction) as well as dark-field contrast (due to small-angle scattering), thus allowing the study of structures whose sizes are below the resolution of the detector [49]. For example, dark-field enables the study of the wall between two magnetic domains for high-permeability steel laminates. Through phase contrast it is possible, for example, to distinguish Copper and Titanium where the neutron attenuation contrast is modest by virtue of their different refractive index. Finally, by studying the change in orientation of polarised neutrons it is possible to study the fundamental magnetic properties and basic phenomena in condensed matter, such as the characterisation of magnetic flux in superconductors below the critical temperature and the skin effect in conductors or magnetic domain distributions in bulk ferromagnets [50].

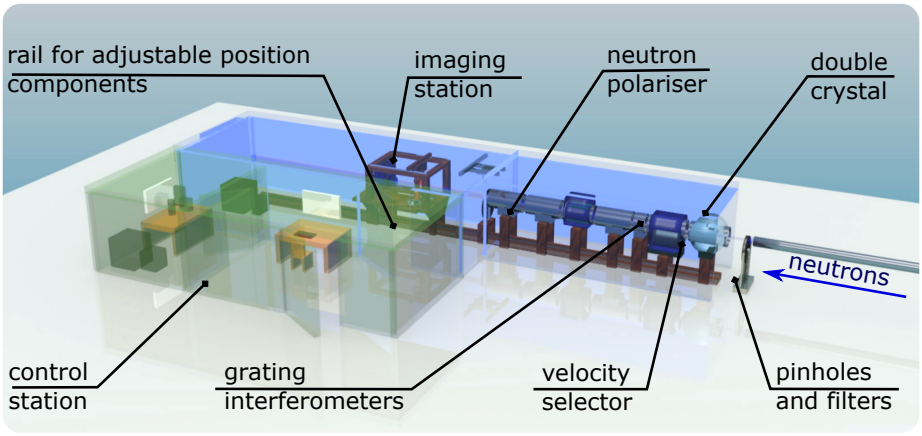

Figure 13: Conceptual drawing of the future upgrade of the instrument.

Acknowledgements

This work is supported by the French National Research Agency in the framework of the "Investissements d'avenir" program (ANR-15-IDEX-02) as well as by the company TOTAL. The authors also wish to thank the members of the Committees of the instrument (in alphabetical order I. Betremieux, J. Desrues, G. Fragneto, G. Galliero, S. Hall, M. Johnson, M. Letiche, P. Moonen, C. Simon, N.C. Tranh) for their help and support. We also wish to thank the help of Nikolay Kardjilov and Jaime Segura, as well as the essential technical support of K. Buckley. Finally, the authors wish to thank the anonymous reviewers for their helpful comments and recommendations, which helped improve the quality of this paper.

References

References

[1] I. Manke, J. Banhart, A. Haibel, A. Rack, S. Zabler, N. Kardjilov, A. Hilger, A. Melzer, H. Riesemeier, In situ investigation of the discharge of alkaline zn–mn o 2 batteries with synchrotron x-ray and neutron tomographies, Applied physics letters 90 (21) (2007) 214102.

[2] C. Hartnig, R. Kuhn, P. Krueger, I. Manke, N. Kardjilov, J. Goebbels, B. R. Mueller, H. Riesemeier, Water management in fuel cells-a challenge for non-desctructive high resolution methods, MATERIALS TESTING 50 (10) (2008) 609–614.

[3] M. Hickner, N. Siegel, K. Chen, D. Hussey, D. Jacobson, M. Arif, In situ high-resolution neutron radiography of cross-sectional liquid water profiles in proton exchange membrane fuel cells, Journal of The Electrochemical Society 155 (4) (2008) B427–B434.

[4] E. H. Lehmann, P. Boillat, A. Kaestner, P. Vontobel, D. Mannes, Neutron imaging methods for the investigation of energy related materials-fuel cells, battery, hydrogen storage and nuclear fuel, in: EPJ Web of Conferences, Vol. 104, EDP Sciences, 2015, p. 01007.

[5] S. L. Cann, E. Tudisco, C. Perdikouri, O. Belfrage, A. Kaestner, S. Hall, M. Tägil, H. Isaksson, Characterization of the bone-metal implant interface by digital volume correlation of in-situ loading using neutron tomography, Journal of the Mechanical Behavior of Biomedical Materials 75 (2017) 271 – 278. doi:https://doi.org/10.1016/j.jmbbm.2017.07.001.
URL http://www.sciencedirect.com/science/article/pii/S1751616117302874

[6] C. Tötzke, N. Kardjilov, I. Manke, S. E. Oswald, Capturing 3d water flow in rooted soil by ultra-fast neutron tomography, Scientific reports 7 (1) (2017) 6192.

[7] F. Witzmann, H. Scholz, J. Mueller, N. Kardjilov, Sculpture and vascularization of dermal bones, and the implications for the physiology of basal tetrapods, Zoological Journal of the Linnean Society 160 (2) (2010) 302–340.

[8] M. Laaß, B. Schillinger, Reconstructing the auditory apparatus of therapsids by means of neutron tomography, Physics Procedia 69 (2015) 628–635.

[9] E. Stavropoulou, E. Andò, A. Tengattini, M. Briffaut, F. Dufour, D. Atkins, G. Armand, Liquid water uptake in unconfined callovo oxfordian clay-rock studied with neutron and x-ray imaging, Acta Geotechnica (2018) 1–15.

[10] D. Dauti, A. Tengattini, S. Dal Pont, N. Toropovs, M. Briffaut, B. Weber, Analysis of moisture migration in concrete at high temperature through in-situ neutron tomography, Cement and Concrete Research 111 (2018) 41–55.

[11] M. Strobl, I. Manke, N. Kardjilov, A. Hilger, M. Dawson, J. Banhart, Advances in neutron radiography and tomography, Journal of Physics D: Applied Physics 42 (24) (2009) 243001.

[12] N. Kardjilov, I. Manke, R. Woracek, A. Hilger, J. Banhart, Advances in neutron imaging, Materials Today 21 (6) (2018) 652–672.

[13] J. LaManna, D. Hussey, E. Baltic, D. Jacobson, Neutron and x-ray tomography (next) system for simultaneous, dual modality tomography, Review of Scientific Instruments 88 (11) (2017) 113702.

[14] A. Tengattini, D. Atkins, B. Giroud, E. Ando, B. J, G. Viggiani, Next-grenoble, a novel facility for neutron and x-ray tomography in grenoble, Proceedings of ICTMS2017-163 88 (03).

[15] E. Tudisco, C. Jailin, A. Mendoza, A. Tengattini, E. Andò, S. A. Hall, G. Viggiani, F. Hild, S. Roux, An extension of digital volume correlation for multimodality image registration, Measurement Science and Technology 28 (9) (2017) 095401.

[16] R. Cubitt, J. Segura Ruiz, W. Jark, Rainbows: refractive analysis of the incoming neutron beam over the white spectrum. a new fast neutron reflectometry technique exploiting a focusing prism, Journal of Applied Crystallography 51 (2) (2018) 257–263.

[17] ISNR, IAEA, Neutron imaging facilities survey, Tech. rep., International Agency of Atomic Energy and International Society for NEutron Radiography (2015).

[18] E. Calzada, F. Gruenauer, M. Mühlbauer, B. Schillinger, M. Schulz, New design for the antares-ii facility for neutron imaging at frm ii, Nuclear Instruments and Methods in Physics Research Section A: Accelerators, Spectrometers, Detectors and Associated Equipment 605 (1-2) (2009) 50–53.

[19] M. Arif, D. Hussey, E. Baltic, D. Jacobson, Neutron imaging facility development and research trend at nist, Physics Procedia 69 (2015) 210–217.

[20] A. Kaestner, S. Hartmann, G. Kühne, G. Frei, C. Grünzweig, L. Josic, F. Schmid, E. Lehmann, The icon beamline–a facility for cold neutron imaging at sinq, Nuclear Instruments and Methods in Physics Research Section A: Accelerators, Spectrometers, Detectors and Associated Equipment 659 (1) (2011) 387–393.

[21] V. Cristiglio, B. Giroud, L. Didier, B. Demé, D16 is back to business: more neutrons, more space, more fun, Neutron News 26 (3) (2015) 22–24.

[22] A. Vorobiev, A. Devishvilli, G. Palsson, H. Rundlöf, N. Johansson, A. Olsson, A. Dennison, M. Wollf, B. Giroud, O. Aguettaz, et al., Recent upgrade of the polarized neutron reflectometer super adam, Neutron News 26 (3) (2015) 25–26.

[23] P. Trtik, E. H. Lehmann, Isotopically-enriched gadolinium-157 oxysulfide scintillator screens for the high-resolution neutron imaging, Nuclear Instruments and Methods in Physics Research Section A: Accelerators, Spectrometers, Detectors and Associated Equipment 788 (2015) 67–70.

[24] C. Tötzke, N. Kardjilov, N. Lenoir, I. Manke, S. E. Oswald, A. Tengattini, What comes next?–high-speed neutron tomography at ill, Optics Express 27 (20) (2019) 28640–28648.

[25] B. R. Müller, A. Lange, M. Harwardt, M. P. Hentschel, B. Illerhaus, J. Goebbels, J. Bamberg, F. Heutling, X-ray refraction topography and computed tomography for nde of lightweight materials (keynote paper), in: Testing, Reliability, and Application of Micro-and Nano-Material Systems III, Vol. 5766, International Society for Optics and Photonics, 2005, pp. 1–9.

[26] S. Williams, A. Hilger, N. Kardjilov, I. Manke, M. Strobl, P. Douissard, T. Martin, H. Riesemeier, J. Banhart, Detection system for microimaging with neutrons, Journal of Instrumentation 7 (02) (2012) P02014.

[27] I. Manke, C. Hartnig, M. Grünerbel, W. Lehnert, N. Kardjilov, A. Haibel, A. Hilger, J. Banhart, H. Riesemeier, Investigation of water evolution and transport in fuel cells with high resolution synchrotron x-ray radiography, Applied Physics Letters 90 (17) (2007) 174105.

[28] P. Trtik, E. H. Lehmann, Progress in high-resolution neutron imaging at the paul scherrer institut-the neutron microscope project, in: Journal of Physics: Conference Series, Vol. 746, IOP Publishing, 2016, p. 012004.

[29] P. Trtik, M. Meyer, T. Wehmann, A. Tengattini, D. Atkins, E. Lehmann, M. Strobl, Psi 'neutron microscope'at ill-d50 beamline-first results, Neutron Radiography: WCNR-11 15 (2020) 23.

[30] D. S. Hussey, J. M. LaManna, E. Baltic, D. L. Jacobson, Neutron imaging detector with 2 μm spatial resolution based on event reconstruction of neutron capture in gadolinium oxysulfide scintillators, Nuclear Instruments and Methods in Physics Research Section A: Accelerators, Spectrometers, Detectors and Associated Equipment 866 (2017) 9–12.

[31] C. Grünzweig, G. Frei, E. Lehmann, G. Kühne, C. David, Highly absorbing gadolinium test device to characterize the performance of neutron imaging detector systems, Review of Scientific instruments 78 (5) (2007) 053708.

[32] S. HALL, M. BORNERT, J. DESRUES, Y. PANNIER, N. LENOIR, G. VIGGIANI, P. BéSUELLE, Discrete and continuum analysis of localised deformation in sand using x-ray µct and volumetric digital image correlation, Géotechnique 60 (5) (2010) 315–322. arXiv:https://doi.org/10.1680/geot.2010.60.5.315, doi:10.1680/geot.2010.60.5.315.
URL https://doi.org/10.1680/geot.2010.60.5.315

[33] A. Kaestner, M. Morgano, J. Hovind, E. Lehmann, Bimodal imaging using neutrons and x-rays, in: Proceedings of the International Symposium on Digital Industrial Radiology and Computed Tomography, http://www.ndt. net/events/DIR2015/Paper/58_Kaestner. pdf (last access: 19 August 2016), 2015.

[34] A. Kaestner, J. Hovind, P. Boillat, C. Muehlebach, C. Carminati, M. Zarebanadkouki, E. Lehmann, Bimodal imaging at icon using neutrons and x-rays, Physics Procedia 88 (2017) 314–321.

[35] E. Tudisco, S. Hall, E. M. Charalampidou, N. Kardjilov, A. Hilger, H. Sone, Full-field measurements of strain localisation in sandstone by neutron tomography and 3d-volumetric digital image correlation, Physics Procedia 69 (2015) 509–515.

[36] M. Etxegarai, E. Tudisco, A. Tengattini, S. Hall, G. Viggiani, Hydromechanical behaviour of porous rock studied with neutron tomography, Proceedings of ICTMS2017-163 88 (03).

[37] H. Lewis, A. Tengattini, G. Couples, E. Tudisco, E.-M. Charalampidou, S. Hall, K. Edlmann, E. Ando, M. Etxegarai, Neutron radiography and tomography used to characterise water flow through a low permeability carbonate altered by experimentally induced fractures, Proceedings of ICTMS2017-163 88 (03).

[38] M. Yehya, E. Andò, F. Dufour, A. Tengattini, Fluid-flow measurements in low permeability media with high pressure gradients using neutron imaging: Application to concrete, Nuclear Instruments and Methods in Physics

Research Section A: Accelerators, Spectrometers, Detectors and Associated Equipment 890 (2018) 35–42.

[39] S. Roshankhah, J. Marshall, A. Tengattini, E. Ando, V. Rubino, A. Rosakis, G. Viggiani, J. Andrade, Neutron imaging: a new possibility for laboratory observation of hydraulic fractures in shale?, Géotechnique Letters 8 (4) (2018) 316–323.

[40] E. Roubin, E. Andò, S. Roux, The colours of concrete as seen by x-rays and neutrons, Cement and Concrete Composites (2019) 103336.

[41] E. Stavropoulou, E. Andò, E. Roubin, N. Lenoir, A. T. M.Briffaut, P. Besuelle, Dynamics of water absorption in callovo-oxfordian clayrock revealed with multimodal x-ray and neutron tomography, Frontiers in Earth Science (accepted).

[42] N. Lenoir, M. Bornert, J. Desrues, P. Bésuelle, G. Viggiani, Volumetric digital image correlation applied to x-ray microtomography images from triaxial compression tests on argillaceous rock, Strain 43 (3) (2007) 193–205.

[43] S. A. Hall, M. Bornert, J. Desrues, Y. Pannier, N. Lenoir, G. Viggiani, P. Bésuelle, Discrete and continuum analysis of localised deformation in sand using x-ray [mu] ct and volumetric digital image correlation, Géotechnique 60 (5) (2010) 315.

[44] E. Andò, S. A. Hall, G. Viggiani, J. Desrues, P. Bésuelle, Grain-scale experimental investigation of localised deformation in sand: a discrete particle tracking approach, Acta Geotechnica 7 (1) (2012) 1–13.

[45] N. Kardjilov, I. Manke, A. Hilger, M. Strobl, J. Banhart, Neutron imaging in materials science, Materials Today 14 (6) (2011) 248–256.

[46] N. Kardjilov, A. Hilger, I. Manke, R. Woracek, J. Banhart, Conrad-2: the new neutron imaging instrument at the helmholtz-zentrum berlin, Journal of Applied Crystallography 49 (1) (2016) 195–202.

[47] E. Lehmann, G. Frei, P. Vontobel, L. Josic, N. Kardjilov, A. Hilger, W. Kockelmann, A. Steuwer, The energy-selective option in neutron imaging, Nuclear Instruments and Methods in Physics Research Section A: Accelerators, Spectrometers, Detectors and Associated Equipment 603 (3) (2009) 429–438.

[48] R. Woracek, J. Santisteban, A. Fedrigo, M. Strobl, Diffraction in neutron imaging—a review, Nuclear Instruments and Methods in Physics Research Section A: Accelerators, Spectrometers, Detectors and Associated Equipment 878 (2018) 141–158.

[49] M. Strobl, R. P. Harti, C. Grünzweig, R. Woracek, J. Plomp, Small angle scattering in neutron imaging—a review, Journal of Imaging 3 (4) (2017) 64.

[50] M. Strobl, H. Heimonen, S. Schmidt, M. Sales, N. Kardjilov, A. Hilger, I. Manke, T. Shinohara, J. Valsecchi, Polarization measurements in neutron imaging, Journal of physics d-applied physics 52 (12) (2019) 123001.